

## 2.1 数据转化知识

### 2.1.1

- (1) 必要；
- (2) 全部必要，数据完整准确；
- (3) 是；是。

## 2.2 结果部分

### 2.2.1

- (1)
- (2)

#### 1.Results

##### 1.1 Profile analysis

By comparing the near-well borehole data and the resistivity inversion results, we established a relationship between the lithology and electrical properties of the sedimentary layers. This relationship is illustrated in Lines 1 and 8 in an adjacent area.

Figure 6a shows the inversion resistivity profile of Line 1 through the analysis of wells QZ584, YL10 and QZ691 located nearby. The significant lateral resistivity contrast on both sides of point 12 000 (figure 6a) suggests the presence of different lithologies. South of this point, the strata can be divided into two layers. The upper layer shows relatively low resistance and consists of roadbed and clay. The lower layer shows high resistivity and consists of limestone and andesite. The strata to the north of point 12 000 can be divided into four layers with distinct electrical characteristics. They exhibit, from top to bottom, a succession of low, high, low and very low resistivity. The resistivity of the upper layer is not uniform, with low overall

resistance and some high resistance areas. The areas of high resistance are thought to result from the subgrade landfill, while the low resistance areas are mainly clay. The underlying relatively thin layer of high resistivity is a sand layer, which is missing in some areas and is the main target of this study. The third, thicker layer is a silty clay and sandy clay layer that shows a lower resistivity than the sand layer. The basal layer is interpreted as bedrock and shows low resistivity. This layer can be further divided into a low resistivity layer and a very low resistivity layer, which correspond to sandstone and mudstone, respectively. The interpreted stratigraphic section of Line 1 is shown in figure 4b.

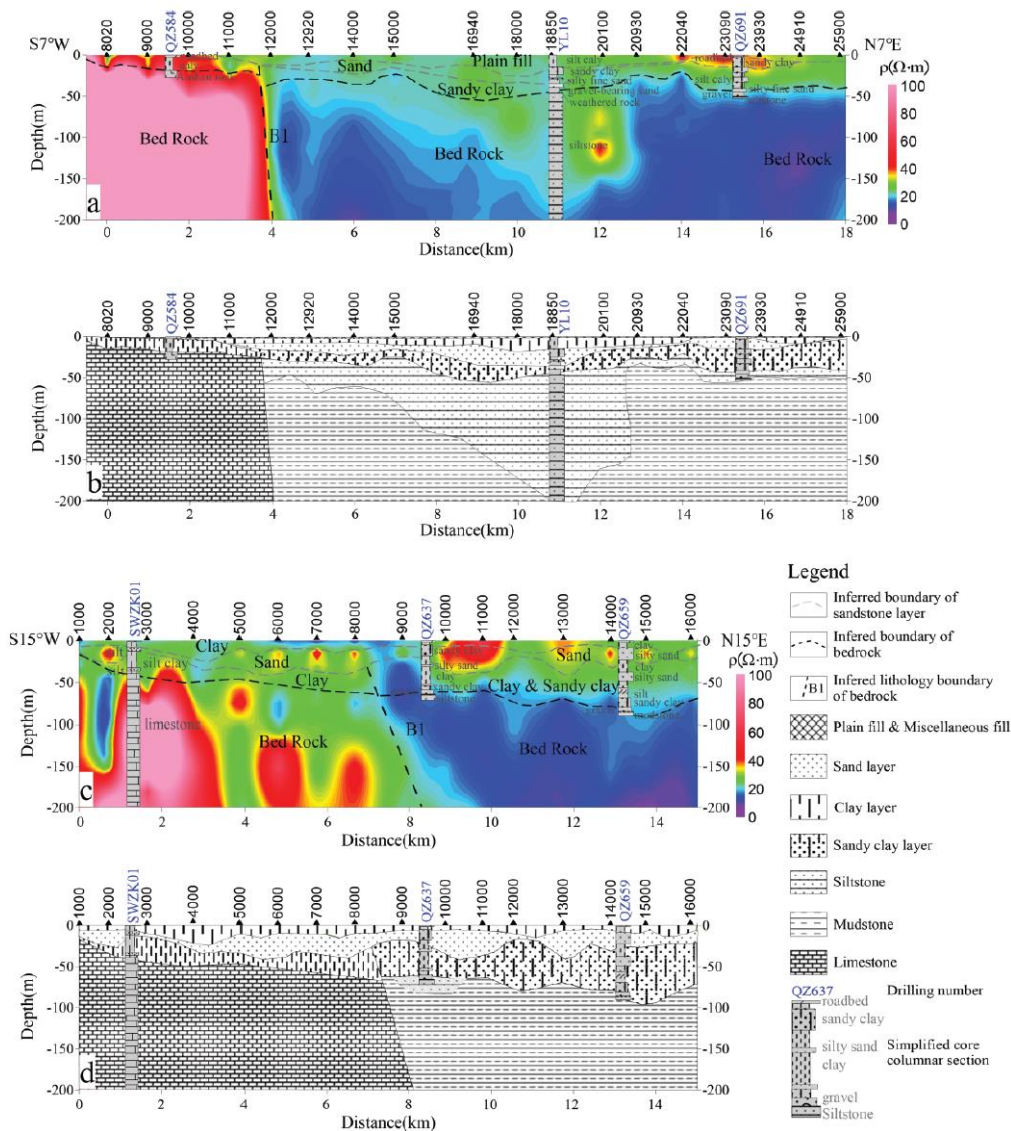


Figure 6. Observed and interpreted resistivity profiles of Line 1 and Line 8 (see figure 2 for locations); (a) inversion resistivity profile of Line 1; (b) inferred geological profile of Line

1; (c) inversion resistivity profile of Line 8 and (d) inferred geological profile of Line 8.

The results of Line 8 (figure 6c) are similar to those of Line 1. The strata can be divided into four lithological units, namely, from the top to bottom, plain fill and clay, sand, clay and sand clay, and bedrock. The results clearly highlight a shallow high-resistivity layer (figure 6d). An obvious difference in resistivity can be seen near point 8000. A distinct difference in bedrock lithology can be recognized on both sides of this point.

Figure 7 illustrates the inversion results of all 15 profiles in the form of 3D slices. The inversion results of each section have a good fitting. The bedrock in the study area is mainly classified into high resistance limestone strata and low resistance siltstone and mudstone. The boundaries between these lithology, projected to the surface, are indicated by the red dotted lines. In the western region, the limestone is mainly in the south and gradually extends to the northeast. Drill hole QZ602, located between sections 3 and 4, is located at the intersection of the limestone basement and siltstone basement, which has highly possibility to have limestone at the corresponding depth. Compared with the sand layers are thinner in the western region (1–6 section range) than in the eastern region (7–15 section range), and even absent in some areas. In the eastern region, the intermediate and shallow strata have relatively higher resistivity. This information is fundamental for dividing the Quaternary loose sediments in our study area. Moreover, the thickness of this sand layer exhibits spatial variation.

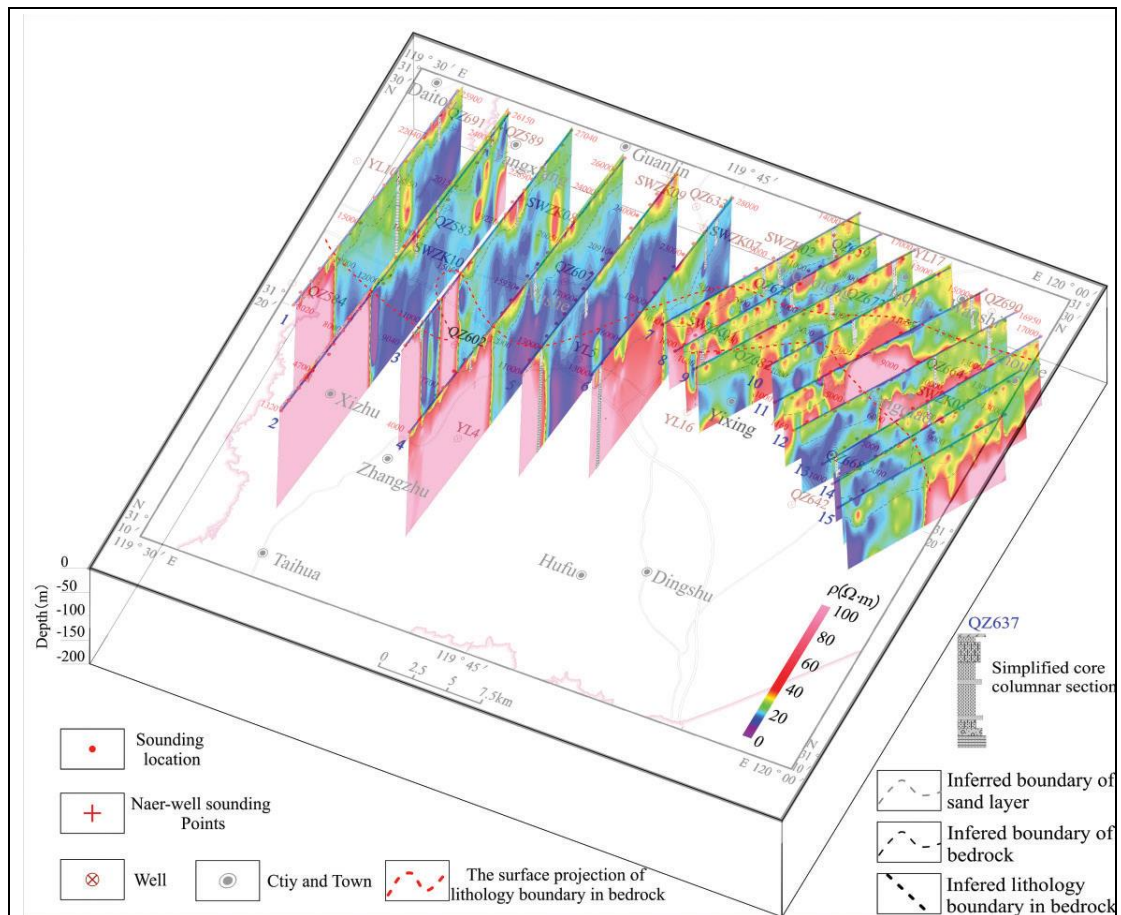


Figure 7. 3D fence diagram of the inversion results of 15 profiles in the study area.

### 1. Plane analysis and geological modeling

Based on the interpretation of all lines (figure 7), and on a comprehensive comparison of the electrical characteristics (through a correlation of similar electrical characteristics across adjacent lines), the spatial distribution of the sand layer thickness in the study area was obtained (figure 8). Figure 8 shows that along the Xizhu–Xushe–Yangxiang–Daitou line and around the downtown areas of Yixing and Fangqiao the sand layer is thin or even absent in places. In contrast, along the Gaoteng–Heqiao–Wanshi–Zhoutie line, the sand layer is >30 m thick.

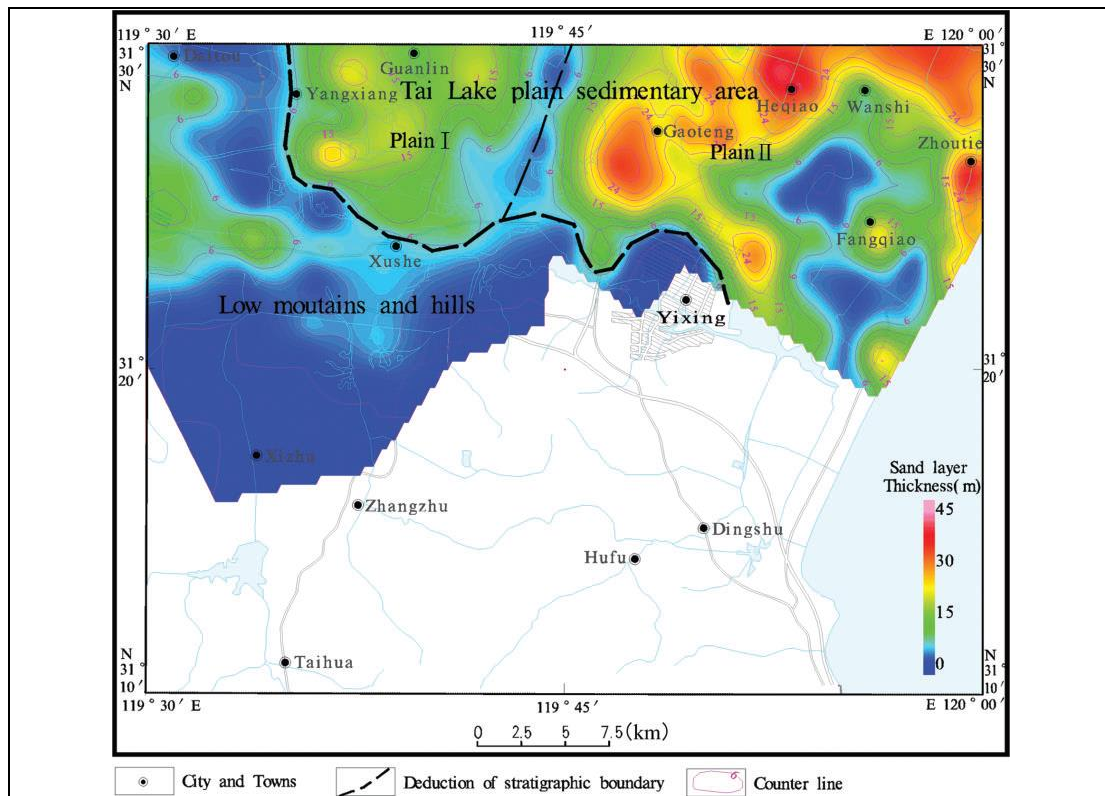


Figure 8. Isopach map of sand layer thickness in the study area.

Based on resistivity inversion results and drilling data in the study area, a 3D geological model of bedrock and sand-bearing strata in the region is established and calibrated shown in figure 9. The well-calibrated bedrock geological model is composed of multiple lithologic types, such as limestone, sandstone and mudstone, by resistivity characteristics. One can see that the bedrock in the study area gradually deepens from the southwest mountain to the northeast Tai Lake. Meanwhile, the limestone, sandstone and mudstone alternate within the bedrock. According to the general rule that the larger the sand grain size, the higher the resistivity (Winsauer et al. 1952), the sand-bearing strata were divided into silty sand, fine sand, medium sand, coarse sand and gravel according to their inversion resistivity.

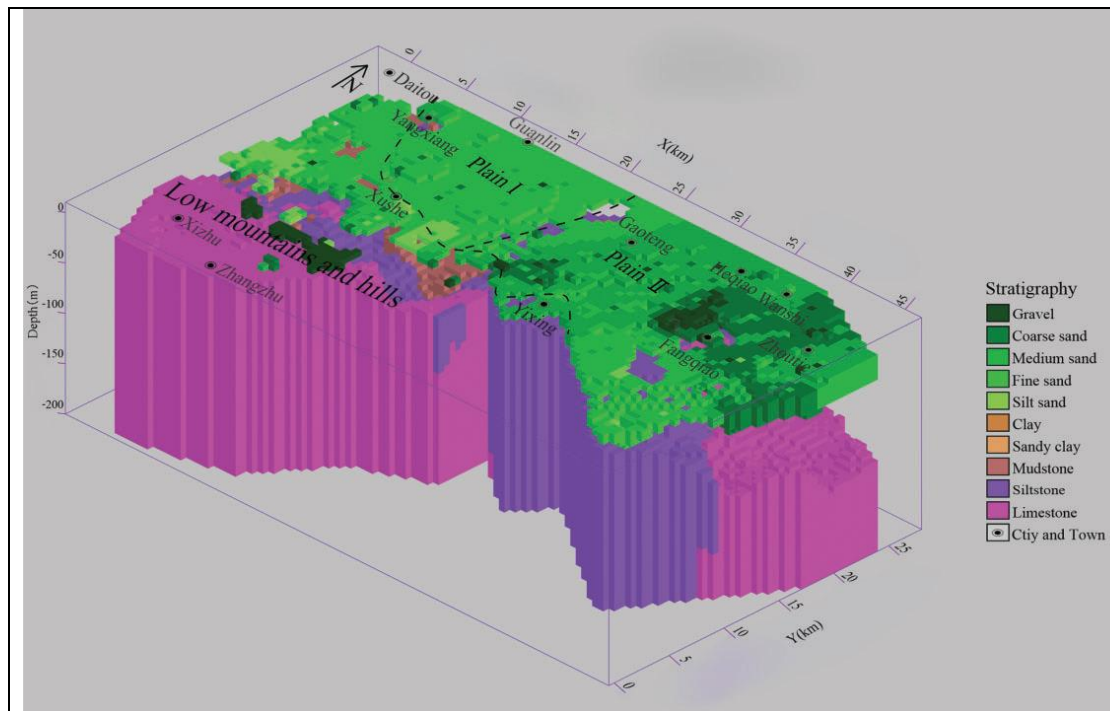


Figure 9. 3D geological model of bedrock and sand layers in the study area.

The significant variation in the thickness of the sand was interpreted as evidence of two distinct depositional zones. These two zones are demarcated by the black dotted line in figures 8 and 9. The sand layer in the southern region (thilly area) was thinner (or even absent) and the bedrock was shallower. In the northern area, which borders Tai Lake to the east, the sand layer was thick and contained loose sediments deposited during the Quaternary. The sand layer gradually thickened, and the grain size gradually increased from the southwest to the northeast. We identified this area as the Tai Lake plain depositional area via geological analysis. Based on the thickness and grain size, we further divided this area into two subregions, i.e. the Tai Lake sedimentary plains I and II.

As can be observed from figure 10, our proposed classification is generally consistent with that of the regional Geology of Jiangsu and Shanghai (Bureau 1984) and with the stratigraphic memoir of the lower-middle Yangtze valley (Chen & Wu 1989). However, differences are evident at a small scale, which are more consistent with the regional Geology of Jiangsu and Shanghai (Bureau 1984). In this study, the boundaries of the areas are more accurate, which improves the previous understanding of the Quaternary stratigraphic subregions.

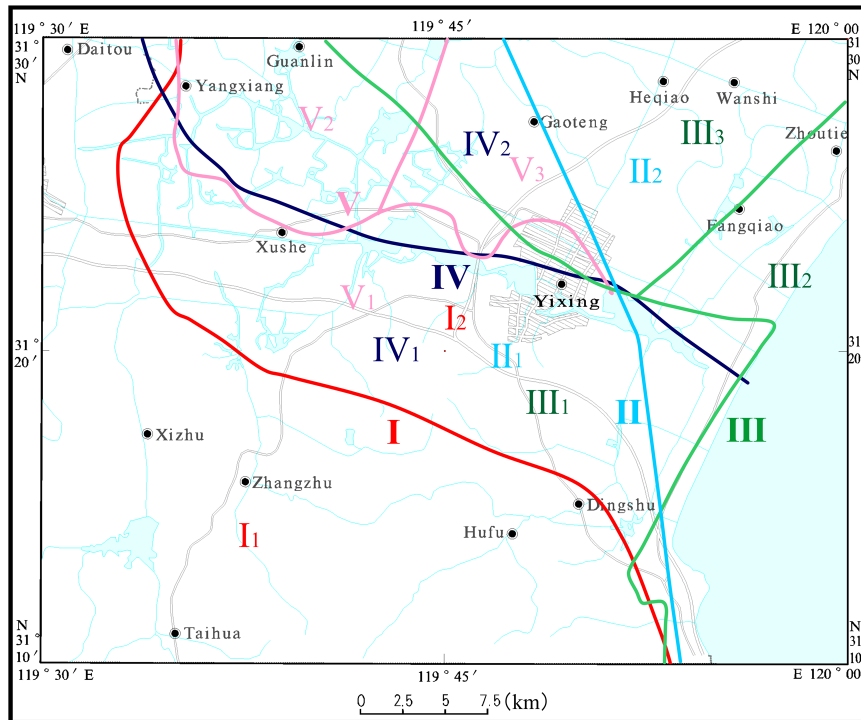


Figure 10. Comparison of Quaternary stratigraphic division schemes in the study area. Solid lines in different colors represent the boundary of the Quaternary stratigraphic subregions according to different scholars in different periods. The specific divisions are interpreted as follows (numbers colored according to the lines that specify the stratigraphic divisions): I Wu (1987): I1 peripheral strata area, I2 Tai Lake strata area; II Chen & Wu (1989): II1 hill-terrace sedimentary plain of the low-middle Yangtze valley, II2 sedimentary area of the Yangtze Delta Plain; III Miao et al. (2016): III1 Nanjing-Yixing low mountains and hills, III2 Changzhou-Wuxi plain, III3 hilly area of southern Jiangyin around Tai Lake; IV Bureau of Geology and Mineral Resources of Jiangsu Province (Bureau 1984): IV1 southwestern low mountains and hills, IV2 Yangtze Delta Plain; V present study: V1 southwest low mountains and hills area, V2 Tai Lake plain sedimentary area and V3 Tai Lake plain II.

## 2. Verification with coring data

The sedimentary area of Tai Lake plain was divided into two subregions, which are indicated by the black dotted line in figure 8. The comparison among drilling data from YXZT44 and YXZT11 in the Tai Lake plain sedimentary area (figure 11) highlights obvious differences in lithological characteristics between the eastern and western sides, especially in strata of the middle and early stage of the late Pleistocene

and older (the depth of this layer is ~30–40 m but decreases to ~20 m in some areas). In the western region, the large loess clay suite of the Xiashu Formation was relatively developed, whereas the corresponding sand layer was thin (as shown by the lithology of YXZT47 and XZT44 in figure 11). In the eastern region, gray silt clay and silty sand were relatively developed and contained fossils. The sedimentary strata had the characteristics of a lagoon-estuary environment and the corresponding sand layer was relatively thick. Through a comparison of the lithological and coring data from plain I and plain II, distinct differences can be observed. These differences support the subdivision of the Tai Lake plain area and demonstrates that the results of the DC method are consistent with coring data in this area.

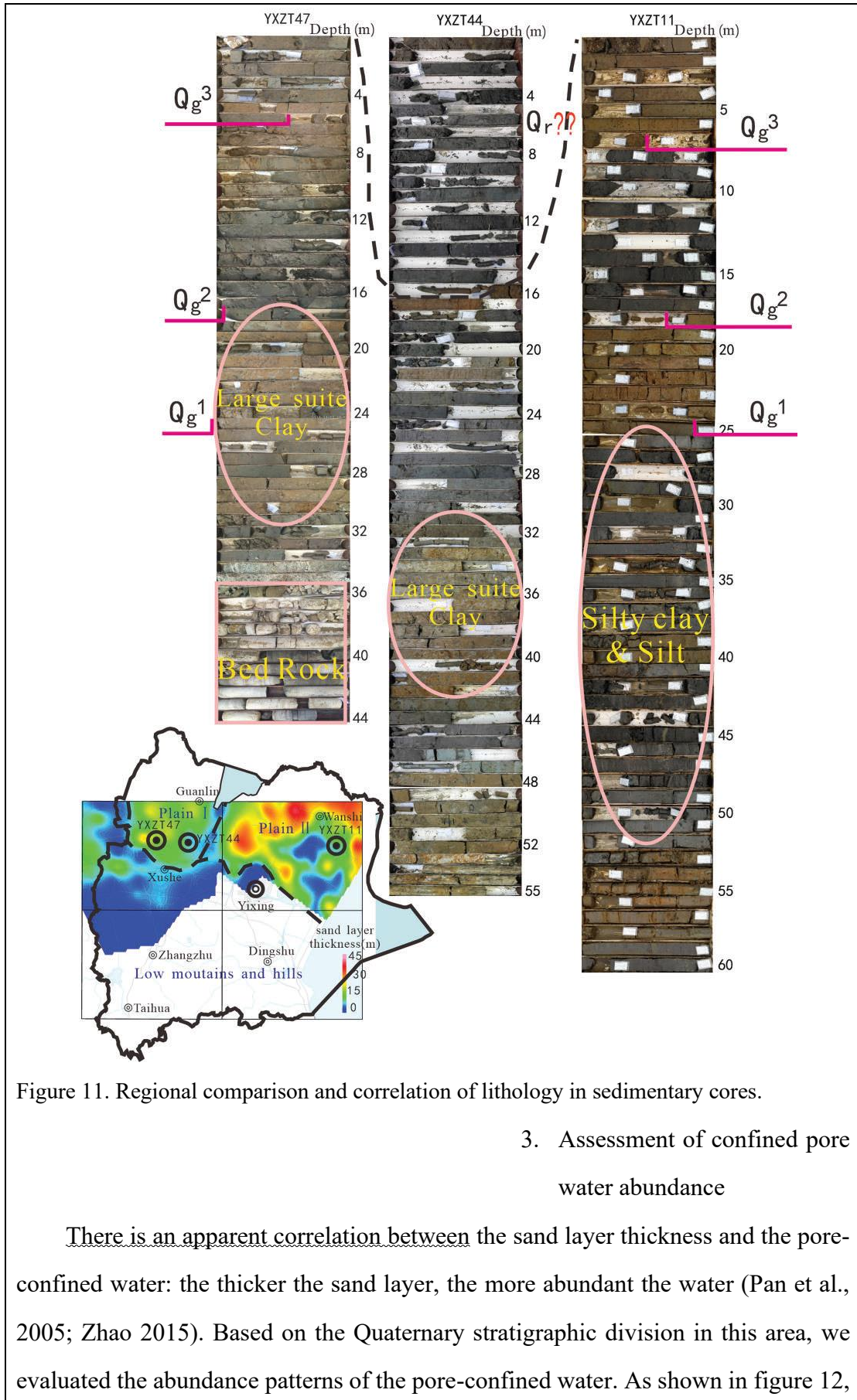


Figure 11. Regional comparison and correlation of lithology in sedimentary cores.

### 3. Assessment of confined pore water abundance

There is an apparent correlation between the sand layer thickness and the pore-confined water: the thicker the sand layer, the more abundant the water (Pan et al., 2005; Zhao 2015). Based on the Quaternary stratigraphic division in this area, we evaluated the abundance patterns of the pore-confined water. As shown in figure 12,

water was most abundant in the northeastern region, i.e. in the Quaternary stratigraphic subdivision corresponding to the Tai Lake plain II, where the sand layer thickness exceeded 25 m. In contrast, in the Tai Lake plain I (where the sand layer thickness was 15–25 m), a water-poor area could be seen in the low hilly land in the Quaternary stratigraphic classification. Based on these features, we suggest that the underground water source for the city of Yixing should be sought in the Tai Lake plain areas II or I but not in the hilly region.

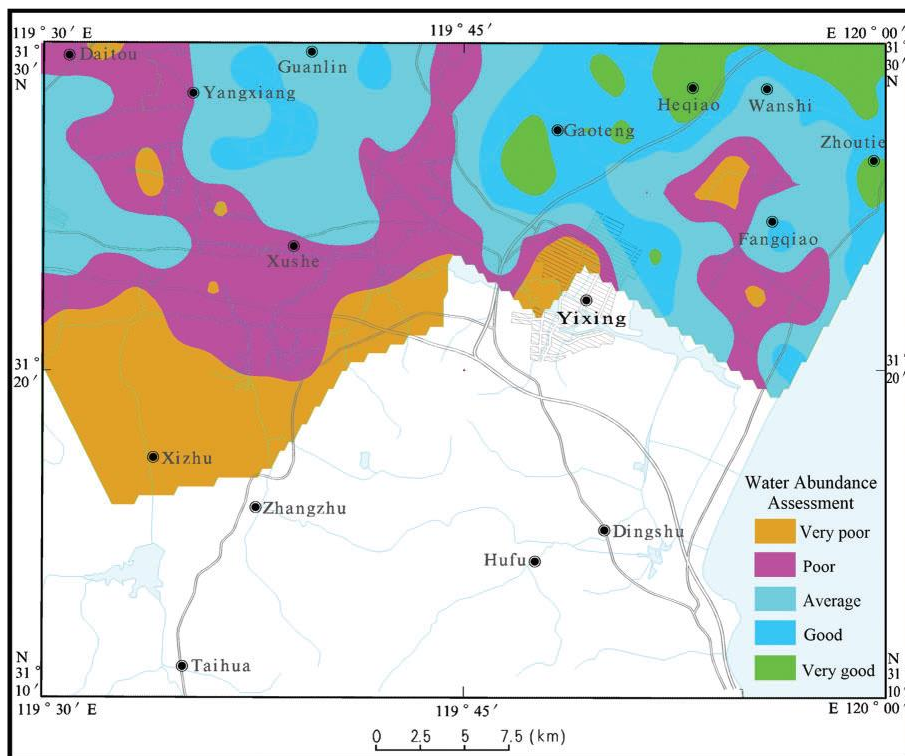


Figure 12. Map showing the distribution of the favorable regions of the inferred enriched confined pore water in the study area: very poor ( $T < 1\text{m}$ ); poor ( $1 < T < 5\text{m}$ ); average ( $5 < T < 15\text{m}$ ); good ( $15 < T < 25\text{m}$ ); very good ( $T > 25\text{m}$ ) and  $T$  represents the thickness of the sand layer.

## 2. Results and Discussion

We will focus our analysis on Model B, which appears to provide the best fit to the data. Model A and Model C will be used to investigate the effect of changing the number of model layers, and Model D will provide a reference for the efficiency of the NUTS algorithm.

The traces of MCMC samples in Fig. 2 for the variables  $\rho_1$  and  $\rho_4$  show that

the parameters have converged to similar distributions across the three chains in Model B. If the chains were noticeably different it would indicate poor convergence. This visual analysis is supported by the  $\hat{R}$  values in Table 1 which are very close to 1.00. The  $\hat{R}$  value is a measure of how similar the separate chains are, with an ideal value of 1.00 for chains which have converged to the same distribution. The fact that several of the variables have  $\hat{R}$  values  $> 1.00$  shows how difficult it is to sample a non-linear MT inversion model, however, the maximum value of  $\hat{R} = 1.02$  is small enough that we can still be confident of convergence.

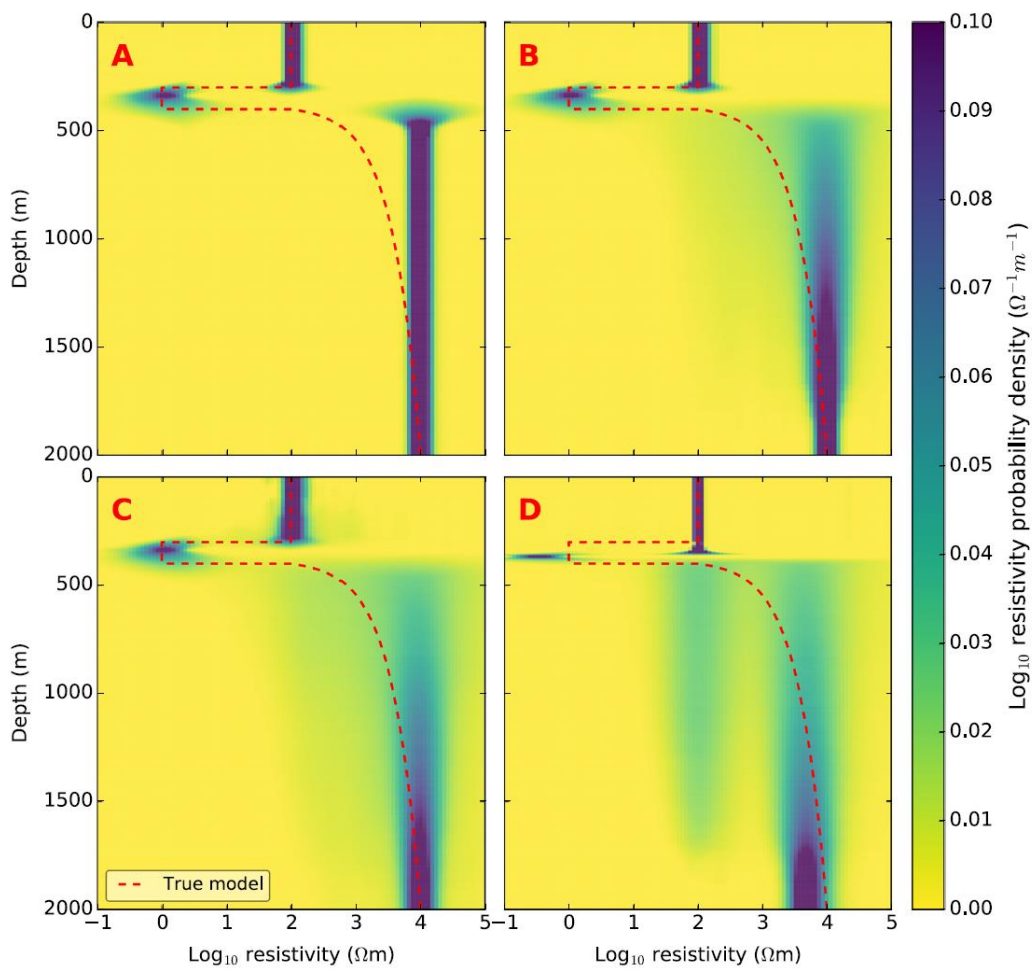


Figure 1 Probability densities generated from the four synthetic probabilistic inversions, each generated using 1500 samples. Shown are four different models; a NUTS sampler, 3 layers b NUTS sampler, 4 layers, c NUTS sampler, 5 layers and d MT-DREAM(ZS) sampler, 4 layers. The dotted red line shows the resistivity profile used to generate the synthetic data. Probability densities are with respect to log<sub>10</sub> resistivity. Densities have been clipped at 0.1

$\Omega^{-1}\text{m}^{-1}$  to allow better visualisation of the lower density areas

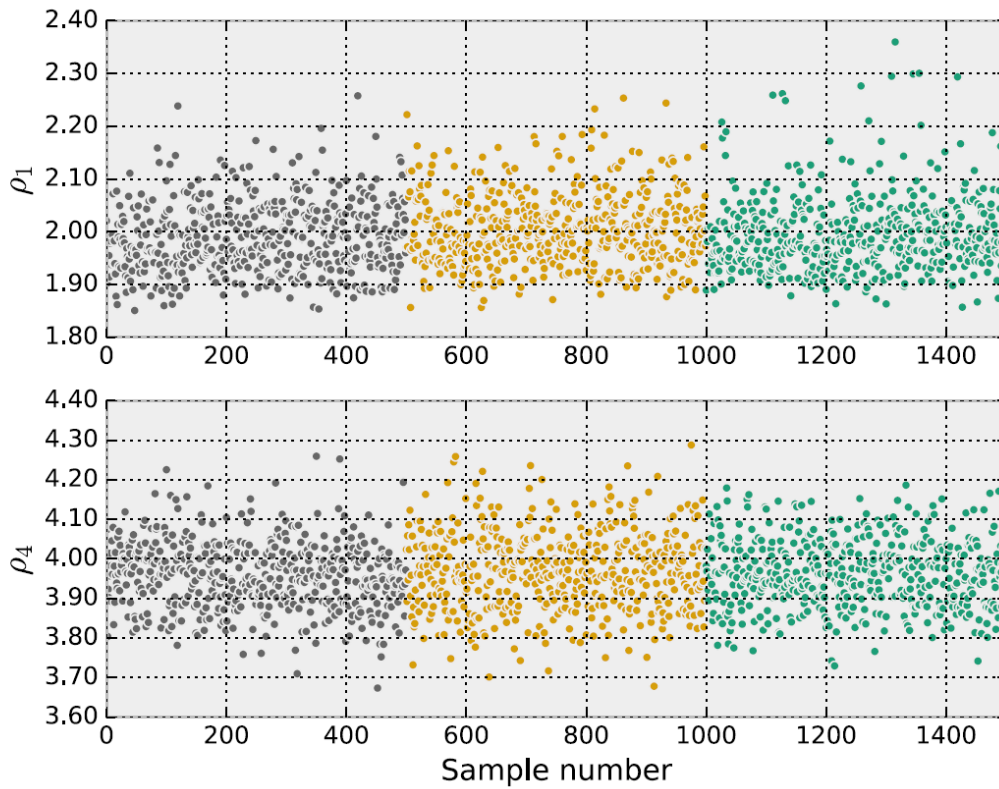


Figure 2 Parameter traces from the synthetic inversion for Model B, showing the sampled  $\log_{10}$  resistivities of the top layer,  $\rho_1$ , and bottom layer  $\rho_4$ . The traces are split into their three chains by colour. Each chain is independent and is given a different random initialisation. Similar distributions between chains is a sign of convergence

The  $\rho$  values for Model B have converged to distributions with means very close to the actual resistivity profile. The resistivity values for  $\rho_1$ ,  $\rho_2$  and  $\rho_4$  have means and standard deviations of  $10^{2.00 \pm 0.07}$ ,  $10^{-0.11 \pm 0.27}$  and  $10^{3.96 \pm 0.09} \Omega \text{ m}$  with target values of  $10^{2.0}$ ,  $10^0$  and  $10^4 \Omega \text{ m}$ , respectively. The layer  $\rho_3$  is a smooth transition between  $\rho_2$  and  $\rho_4$  in the target profile, and as such has no fixed target value.

The  $t$  values given by Model B are also within the ranges of the target model.  $t_1$  and  $t_2$  have distributions of  $307 \pm 15$  and  $88 \pm 45$  m, with target values of 300 and 100 m, respectively.

The  $\beta$  values in the model can serve as a proxy for the probability of a sharp transition in resistivity. The values of  $\beta_1$  and  $\beta_2$  are large enough that they do not

introduce much smoothing. This allows for sharp changes between the layers  $\rho_1$  and  $\rho_2$ , as well as between  $\rho_2$  and  $\rho_3$ . Notably, the 2.5 percentile values for  $\beta_1$  and  $\beta_2$  are 0.91 and 0.90  $\Omega$  m, which indicates that there is a low probability that the layers  $\rho_1$  and  $\rho_2$  have the same resistivities. In contrast, the  $\beta_3$  2.5 percentile is 0.08  $\Omega$  m, which means that there exist models where  $\rho_3$  and  $\rho_4$  are very close, i.e., a three-layer model. The reasonably high mean of 1.73  $\Omega$  m indicate, however, that there are 4-layer models which can better fit the data. The end distribution is a continuous mixture of the two cases. // 【对于实验结果进行文字性描述】

These results are shown graphically in Fig. 1. The inversion accurately maps the top two layers in the profile, with a strong degree of confidence in the boundary location. The second layer is also mapped correctly in thickness and resistivity. The inversion has a large degree of uncertainty underneath the second layer. Here the model can either fit with the basement resistivity immediately, or with a better fitting but more complex model which smoothly changes. Once again, both possibilities have a non-negligible probability, however, the three-layer model has the higher probability.

Figure 3 shows the distribution of apparent resistivity and phase for the 1500 samples. Although each data point is contaminated with an equal magnitude of noise, the model clearly has more confidence in the apparent resistivity and phase at certain periods. The apparent resistivity is most tightly constrained near its minima between 0.1 and 1 s, as well as at 100 s, and the phase has probability density peaks between 0.03 and 0.1 s as well as between 1 and 3 s. These distributions could be used to export new data values and error values as a form of 1D data smoothing. // 【对于实验结果的分析解释】

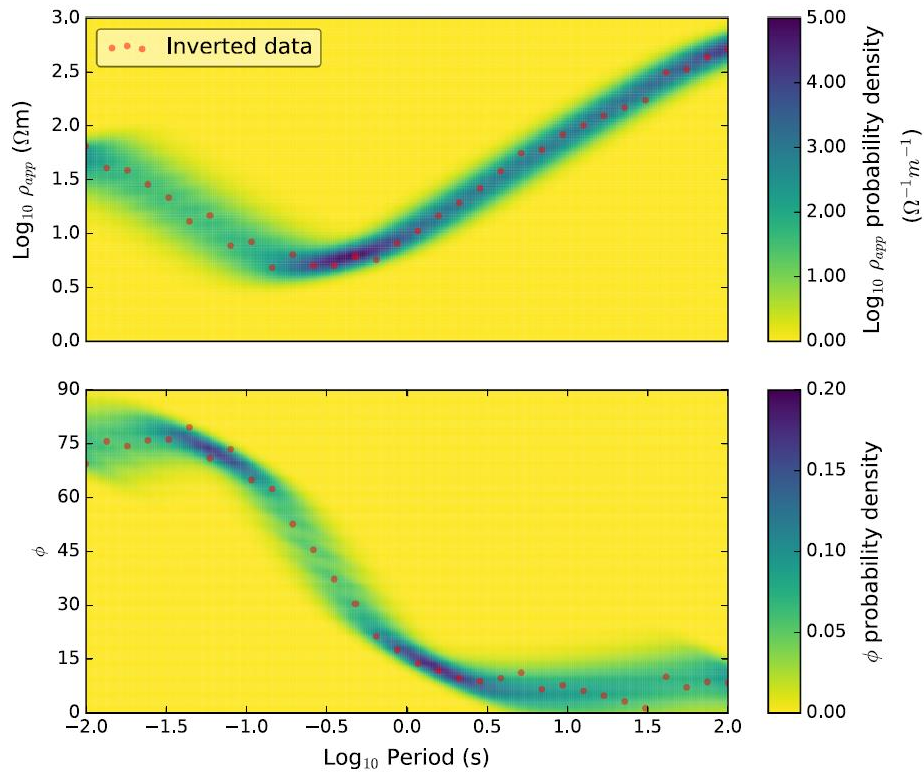


Figure 3 Probability distributions for response curves from the synthetic probabilistic inversion of Model B. Distributions are period independent; the top plot shows probability per  $\log_{10} \rho_{app}$ , the bottom plot probability per phase angle (unitless). Overlain in red are the data points used for the inversion

Comparing Model B with Model A in Fig. 1, we can see that the 3-layer Model A does not have enough flexibility to model the smooth change between the second layer and the basement. But, it still manages to provide accurate resistivities for the top two layers and basement. It is not surprising that a 3-layer model can provide a good fit to the model, as the maximum a posteriori model from the 4-layered Model B is a 3-layered model. The probability densities in Fig. 1 from Model A, however, have a negligible probability in the area where there is a smooth change from the second layer to basement, so it is not as accurate as Model B for modelling this dataset.

The 5-layer inversion in Model C, however, provides a resistivity probability density in Fig. 1 very similar to Model B. The top two layers are identical between the two models, however, there is a slight difference in the smooth transition area,

with Model C favouring slightly more structure. Due to the fact that the regularisation is applied on a layer by layer case rather than looking at the overall structure, increasing the number of layers would allow for slightly rougher models. This could be mitigated by increasing the k parameter for models with more layers. The results from Model A and Model D show that the final model is largely independent of the number of layers in the model, as long as there are enough layers to introduce sufficient structure into the model. If in doubt, it would be reasonable to err on the side of too many layers, as doing so appears to have few deleterious effects apart from a reduction in sampling efficiency. In 2D and 3D smooth inversions the layer geometries are fixed throughout the inversion, so choosing the number of layers is not an issue.

The results from Model D have a much greater contrast with those of Model B. Despite the excellent  $\hat{R}$  convergence statistics for Model D in Table 1, we can see that the distributions are not as accurate as those in Model B. The upper limit of the 95% confidence interval for q1 is exactly the true value of 102:0X m, however, the true values of q2, t1 and t2 all fall outside of their 95% confidence intervals. The basement resistivity q4 is more accurate, however. In the resistivity density plot for Model D shown in Fig. 1, we see probability densities in small areas for the top two layers. This is characteristic of a poor exploration of the model a posteriori, which is common for models with highly correlated parameters. We also see that in the smooth transition zone there appears to be a bimodal distribution between a 3-layer model and a 4-layer model. This characteristic is also present in Model B, however, in there is a smooth reduction in probability with increasing model complexity rather than two strong modes. // 【不同实验模型之间进行对比，提出各模型优缺点】 Coupled with the faster compute time of Model B, we would conclude from these results that NUTS is an excellent choice to sample MT resistivity structures our 1D model. We would further expect the NUTS algorithm to perform well in 2D and 3D spaces, as the sampling efficiency scales well with increased dimensionality. However, further investigation is required to compare it with the MT-DREAM(ZS)

algorithm in 2D and 3D, as the MT-DREAM(ZS) algorithm is designed particularly for higher dimensional problems and is not expected to perform optimally when inverting fewer parameters. This may cause the relative efficiencies to change with increased parameters. // 【对于实验结果进行进一步讨论，选取最佳实验模型，提出改进方向】

Table 1. A comparison summary of the sampled parameters from the synthetic probabilistic inversions of the 4 layer model with NUTS sampler (Model B) and 4 layer model with MT-DREAM(ZS) sampler (Model D)

	Mean	MeanSE	SD	2.5%	50%	97.5%	$n_{\text{eff}}$	$R^{\wedge}$
NUTS sampler—Model B								
$q_1$	2.00	3.4e-3	0.07	1.89	1.99	2.16	421	1.00
$q_2$	- 0.11	0.02	0.27	-	- 0.06	0.29	255	1.00
$q_3$	3.57	0.11	1.40	0.73	3.71	6.54	170	1.02
$q_4$	3.96	3.2e-3	0.09	3.80	3.96	4.15	793	1.00
$t_1$	306	0.88	15.4	274	307	333	302	1.00
$t_2$	90.1	2.69	47.1	17.7	85.9	195	306	1.01
$t_3$	682	17.6	448	34.0	635	1451	650	1.01
$b_1$	2.65	0.05	1.55	0.91	2.27	7.003	1002	1.00
$b_2$	2.81	0.09	2.05	0.90	3.19	8.48	493	1.01
$b_3$	1.69	0.08	1.67	0.06	1.19	6.32	403	1.01
DREAM sampler—Model D								
$q_1$	1.98	2.1e-3	0.09	1.96	1.98	2.00	2074	1.00
$q_2$	- 0.51	7.9e-3	0.22	-	- 0.50	- 0.10	736	1.00
$q_3$	3.07	0.03	1.20	0.88	3.04	5.87	1940	1.00
$q_4$	3.68	5.9e-3	0.35	3.34	3.66	4.10	3554	1.00
$t_1$	355	0.23	6.02	344	356	362	731	1.00
$t_2$	29.5	0.87	22.1	10.9	25.6	64.7	649	1.00
$t_3$	822	7.60	442	52.4	866	1470	3201	1.00
$b_1$	2.98	3.6e-2	1.85	1.03	2.49	7.77	2602	1.00
$b_2$	3.56	3.8e-2	1.90	1.16	3.12	8.53	2549	1.00
$b_3$	1.75	3.1e-2	1.51	0.06	1.41	5.74	2311	1.00

Subscripts indicate increasing layer number. Summaries included are the mean of the distribution; standard error of the mean; standard deviation; percentiles at 2.5, 50, 97.5% (the median and the bounds for the 95% confidence interval); effective sample size estimate;  $R^{\wedge}$ , the potential scale reduction statistic.

(3) 例文 1 的条理更加清晰，该片段中将实验结果部分划分为不同部分，并设置概括性小标题，增加了文章的可读性，使得行文脉络更加清晰。

## 2.3 方法部分

### 2.3.1

类型	Arvin B. Karpiah et al.(2022)
细分式	√
大类式	

在方法部分使用细分式结构，能够使得文章方法部分逻辑清晰，详略得当，重点突出。

### 2.3.2

(1) CSEM Instrumentation; Surveying; Data Processing;

(2) CSEM Instrumentation 对于文章中用到的海洋可控源电磁法仪器系统及其适用条件等进行介绍; Surveying 实验中进行数据采集的各项数据进行介绍; Data Processing 介绍对于采集数据的处理方法

### 2.3.3

略

## 2.4 前言部分

### 2.4.1

Since 1990, Chinese geologists have identified three gas hydrate prospecting basins in the northern slope of the South China Sea (SCS), from west to east (Fig. 1): Qiongdongnan Basin (QB), Pearl River Mouth Basin and Southwest Taiwan Basin (Song et al., 2001; Chen et al., 2004; Wei et al., 2012; Wu et al., 2013). In the Pearl

River Mouth Basin, two phases of drilling (GMGS-I, GMGS-II in Fig. 1) were carried out and hydrate samples were recovered in 2007 and 2013 respectively (Sha et al., 2015). In recent years, seismic bottom simulating reflector (BSR) and mud diapirs have been inferred by seismic reflection data, and biomes communities on seafloor have been found by remote operated vehicle (ROV) and camera observation, which indicate the potential of gas hydrate resource in QB (Yu et al., 2014; He et al., 2016). // 【研究背景】 【已有研究基础】

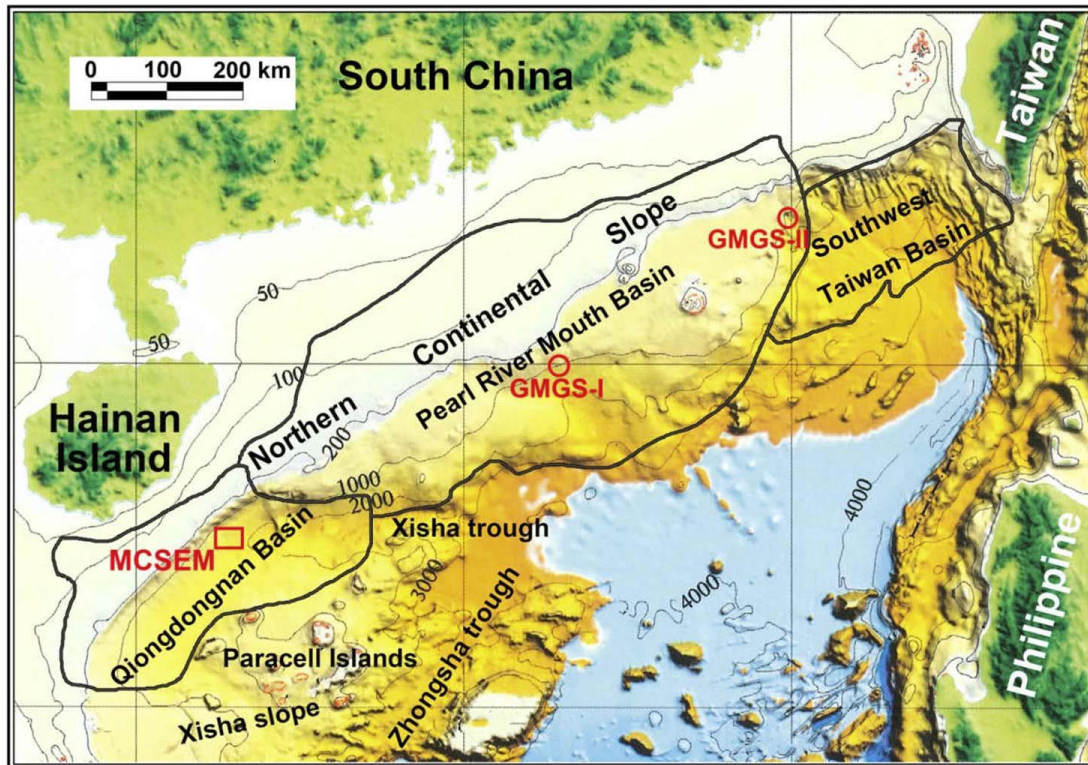


Fig. 1. Location map showing the area of the MCSEM survey in the QB (red rectangle) and the gas hydrate drilling positions of GMGS-I and GMGS-II in the Pearl River Mouth Basin (red open circles), northern slope of the SCS. The base map is from Chen and Wen (2010). (For interpretation of the references to colour in this figure legend, the reader is referred to the web version of this article.)

The BSR is typically interpreted as the boundary between free gases and solid hydrate, whereas the upper reaches of the gas hydrate stability zone (GHSZ) and the distribution of gas hydrate in shallow seabed are not well understood in QB. In addition, it is still difficult to identify the BSR because of the multiple waves, bubble effect, flat seabed and unobvious polarity reversal in seismic reflection data (Yang et

al., 2013; Zhang, 2014). // 【现有工作存在的问题】

Marine controlled-source electromagnetic method (MCSEM), utilizing a horizontal electric dipole source towed close to the seafloor and transmitting an electromagnetic field, is sensitive to horizontal resistors embedded in conductive seabed (Constable and Srnka, 2007). The gas hydrates are orders of magnitude more resistive compared to saline water saturated sediment (Collett and Ladd, 2000), therefore the MCSEM method has been used to image submarine gas hydrate and evaluate the saturation (Yuan and Edwards, 2000; Schwalenberg et al., 2005, 2010; Weitemeyer et al., 2011; Hsu et al., 2014; Goswami et al., 2015, 2016). // 【已有研究基础】

We carried out the first MCSEM survey in QB aimed at mapping marine gas hydrate deposits. This survey is co-located with existing seismic reflection data enabling a joint interpretation. // 【研究目的】 In the study, seafloor electromagnetic receivers were deployed on the seafloor to record electromagnetic fields. The transmitted electromagnetic fields are processed, and an electric section is presented to show lateral resistivity variations across the study area. Integrating MCSEM result with the estimated GHSZ and co-located seismic reflection profile, we discuss the distributions of gas hydrate and free gas in the seabed. // 【本文中拟解决的问题】

## 2.4.2

(1) (2)

Since 1990, Chinese geologists have identified three gas hydrate prospecting basins in the northern slope of the South China Sea (SCS), from west to east (Fig. 1): Qiongdongnan Basin (QB), Pearl River Mouth Basin and Southwest Taiwan Basin (Song et al., 2001; Chen et al., 2004; Wei et al., 2012; Wu et al., 2013). In the Pearl River Mouth Basin, two phases of drilling (GMGS-I, GMGS-II in Fig. 1) were carried out and hydrate samples were recovered in 2007 and 2013 respectively (Sha et al., 2015). // (背景介绍) In recent years, seismic bottom simulating reflector (BSR)

and mud diapirs have been inferred by seismic reflection data, and biomes communities on seafloor have been found by remote operated vehicle (ROV) and camera observation, which indicate the potential of gas hydrate resource in QB (Yu et al., 2014; He et al., 2016).// 【已有研究基础】

The BSR is typically interpreted as the boundary between free gases and solid hydrate, whereas the upper reaches of the gas hydrate stability zone (GHSZ) and the distribution of gas hydrate in shallow seabed are not well understood in QB. In addition, it is still difficult to identify the BSR because of the multiple waves, bubble effect, flat seabed and unobvious polarity reversal in seismic reflection data (Yang et al., 2013; Zhang, 2014).// 【存在问题】

Marine controlled-source electromagnetic method (MCSEM), utilizing a horizontal electric dipole source towed close to the seafloor and transmitting an electromagnetic field, is sensitive to horizontal resistors embedded in conductive seabed (Constable and Srnka, 2007). The gas hydrates are orders of magnitude more resistive compared to saline water saturated sediment (Collett and Ladd, 2000), therefore the MCSEM method has been used to image submarine gas hydrate and evaluate the saturation (Yuan and Edwards, 2000; Schwalenberg et al., 2005, 2010; Weitemeyer et al., 2011; Hsu et al., 2014; Goswami et al., 2015, 2016).// 【已有研究基础】

We carried out the first MCSEM survey in QB aimed at mapping marine gas hydrate deposits. This survey is co-located with existing seismic reflection data enabling a joint interpretation. In the study, seafloor electromagnetic receivers were deployed on the seafloor to record electromagnetic fields. The transmitted electromagnetic fields are processed, and an electric section is presented to show lateral resistivity variations across the study area. // 【研究目的】 Integrating MCSEM result with the estimated GHSZ and co-located seismic reflection profile, we discuss the distributions of gas hydrate and free gas in the seabed. // 【研究意义】

(1) (2)

The aim of magnetotelluric (MT) inversion is to model the subsurface physical properties of the earth based on observations taken at the surface. Geophysical inversion in general is a problem with two halves: an existence problem, where the data are fit by a single earth model which best fits the data, and a uniqueness problem, where all models which fit the data are sought (Backus 1988).// **【研究背景介绍】**

In a Bayesian inversion, the second side of this problem is explored with a model which treats each parameter in the inversion probabilistically, and seeks to find their probability density functions (PDFs) (Tarantola 2005; Tarits et al. 1994). This task is typically achieved with Markov Chain Monte Carlo (MCMC) methods.

The inversion of MT data is an underdetermined problem and requires some form of regularization (Grandis et al. 1999; Schott et al. 1999). In Bayesian inversion, a prior distribution is given for the inversion parameters, which acts to regularise the inversion. Similar to deterministic inversion, the regularisation may take different forms. Common techniques include restricting the number of layers (Guo et al. 2011); calculating the roughness and penalising rougher models with lower probabilities (Grandis et al. 1999; Rosas-Carbajal et al. 2013); or having a variable number of parameters and a penalisation for more complex models (Minsley 2011; Mandolesi et al. 2018).// **【已有研究基础】**

Bayesian inversion of 1D MT data has been successfully applied using MCMC algorithms; however, several challenges exist which make 2D and 3D inversions computationally difficult. These include the reduced speed of the forward algorithms, the slower convergence of the MCMC algorithm with increased number of parameters, and the high covariance of parameters. One solution is to reduce the number of parameters in inversion, e.g., Chen et al. (2012) who used sharp inversions in 2D with a fixed number of nodes. A sharp inversion has the added advantage of avoiding model regularization through smoothness constraints, however, lacks the expressivity of a pixel-based inversion. The first full pixel-based inversion has been implemented for 2D radio magnetotelluric data by Rosas-Carbajal et al. (2013) using

the MT-DREAM(ZS) algorithm (Laloy and Vrugt 2012). The authors show that the algorithm can successfully invert the RMT data, with particularly good results when combined with electrical resistivity tomography in a joint inversion. The inversion is computationally expensive, however, requiring up to 130,000 iterations to reach convergence for 228 model cells, even with prior constraints on resistivity ranges and model roughness. Bayesian inversion has also been used in reduced parameter 3D inversions by Rosas-Carbajal et al. (2015) who used MCMC to invert 7 parameters describing time-lapse changes in resistivity. For a pixel-based 3D MT inversion, the process becomes more difficult, as Grandis (2006) concludes from preliminary studies that a very coarse model mesh would be required to keep computation times reasonable.

One solution to these issues is the use of gradient-based MCMC algorithms based on Hamiltonian mechanics, known as Hamiltonian Monte Carlo (HMC) or Hybrid Monte Carlo. //【研究目的】【现有工作存在的问题】These methods operate by taking a series of steps informed by first-order gradient information (Hoffman and Gelman 2014). This makes them much more efficient than standard MCMC sampling methods such as random-walk Metropolis (Metropolis et al. 1953) and Gibbs sampling (Geman and Geman 1984), with the cost per independent sample from a target distribution of dimensionality  $D$  reduced from  $O(D^2)$  to  $O(D)$  (Creutz 1988). This is clearly advantageous in the case of multi-dimensional MT MCMC inversion, where the number of parameters can run into the thousands.

One of the main obstacles of the HMC algorithms has been the requirement to specify at least two additional parameters to the algorithm, which can have serious effects on sampling efficiency if poorly chosen, and require additional runs to tune correctly. //【现有工作存在的问题】This problem has been solved by the No-U-Turns algorithm (Hoffman and Gelman 2014), an algorithm based on HMC which eliminates the need for specifying tuning parameters. The NUTS algorithm is under active development and has been successfully used in a number of studies in various fields. Some examples include a study of energy consumption from buildings (Chong

et al. 2017), ecological studies investigating populations of various plants and animals (Monnahan et al. 2017) and a supernova study which modelled 9176 parameters (Sanders et al. 2015).// **【已有研究基础】**

We present the first implementation of an MT inversion using the NUTS algorithm. The inversion uses a novel adaptive regularisation scheme which prefers models with smoothly changing resistivities while allowing sharp changes. First, we show the results of a 1D MCMC inversion using NUTS on synthetic data, and highlight the sampling efficiency and model accuracy. Second, we apply the same inversion to MT data obtained from Boulia, Queensland, Australia and show the practical use of the algorithm in geological interpretation. The results show a promising Bayesian inversion which can be upscaled to 2D and 3D MT problems.//

**【本文中拟解决的问题】**

(3) 充足，此文章前言部分引用大量前人文献，说明作者对与相关研究内容了解比较充分。

### 2.4.3

略

## 2.5 讨论与结论

### 2.5.1

#### 6. Discussion

##### 6.1. Thermodynamic estimation of GHSZ

Thermodynamic phase equilibrium has been widely used to calculate the thickness of GHSZ and resources (Rao, 1999; Milkov and Sassen, 2000; Milkov, 2004; Wu et al., 2005; Yu et al., 2014). The thickness of the GHSZ mainly depends on various factors such as bathymetry, sea bottom temperature, geothermal gradient,

pore fluid salinity and the molecular components of gas (Sain et al., 2011). According to the CTD profile (Fig. 7b), the sea-bottom temperature ( $T_0$ ) is approximately 3.2 °C in the survey area. The temperature ( $T$ ) of the seabed, varying with geothermal gradient ( $G$ ) and seabed depth ( $D$ ), can be represented as follows:

$$T = T_0 + G(D - D_w) \quad (1)$$

In this study, the sea water depth ( $D_w$ ) is referred to as 1.35 km.  $G$  is 40 °C/km, which is the average of the study area (Huang, 1999; Wu et al., 2005). // 【 (2) 回顾重要发现】

After analysing the natural gas components in the Ya-13 gas field, Chen et al. (2011) believed that biogenic methane and thermogenic gas exist in the QB. They calculated the phase equilibrium conditions using the CSMHYD program of Sloan and Koh (2008). The thicknesses of the GHSZ for biogenic methane ( $D_{bio}$ ) are different from those of thermogenic gas ( $D_{thermo}$ ). The thicknesses of the GHSZ vary with temperature ( $T$ ) and are as follows (Chen et al., 2011):

$$D_{bio} = 276.23 \exp(0.1106T) \quad (2)$$

$$D_{thermo} = 114.62 \exp(0.185T) \quad (3)$$

Using formulas (1), (2) and (3), we obtain the phase equilibrium curves in the study area (Fig. 12). The thickness of the GHSZ is 320m for biogenic methane and 272m for thermogenic gas. According to the temperature and water depth, we once again calculate the thickness of the GHSZ for methane by using Rao's program (1999). The result is 322 m, which is nearly the same as that of the biogenic methane previously mentioned. // 【 (2) 对比本文研究结果与其他研究人员发现】

Integrating the inversion resistivity model with the calculated GHSZ, we infer that the bottom of the GHSZ is at a depth of 1.67 km, which corresponds to the bottom of layer L2 (dashed line in Fig. 11).

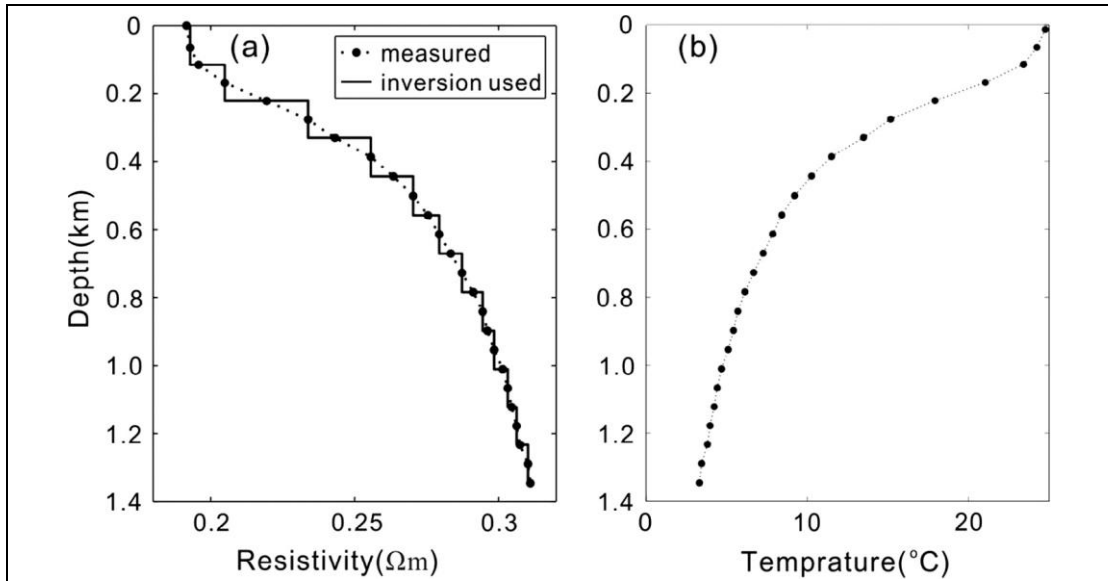


Fig. 7. The conductivity-temperature-depth (CTD) profile of sea water measured in the study area by GMGS. (a) The measured resistivity profile (dotted line) is discretized into 12 layers (stepped line), which have been included in the MCSEM inversion as a fixed structure. (b) The measured temperature profile (dotted line) used in the thermodynamic estimation of GHSZ.

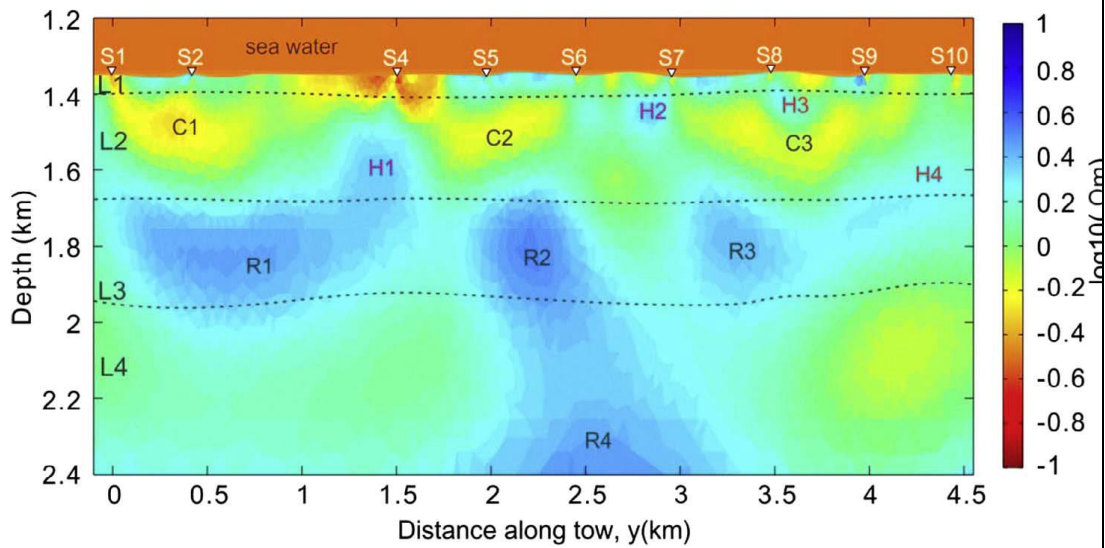


Fig. 11. A close-up view of the inversion model shown in Fig. 10. It has the same scale as the initial model in Fig. 8(b). The white triangles are representative of sites on the seafloor. Black dashed lines are the deduced resistivity interfaces.

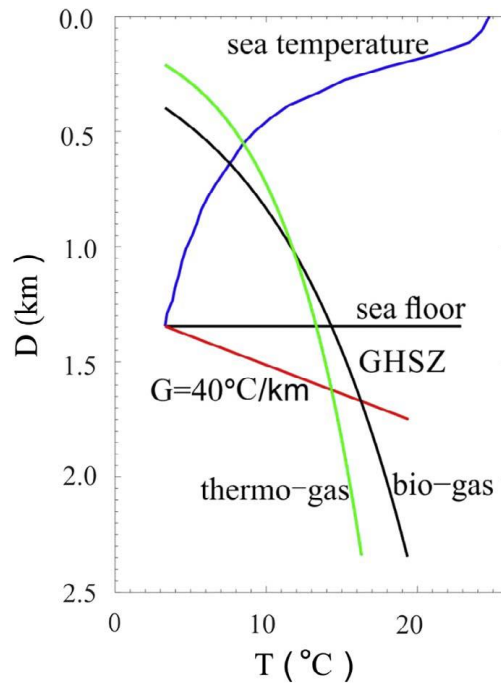


Fig. 12. Phase equilibrium diagram of natural gas hydrates in the study area of the QB. The curve for biogenic methane is referred to as bio-gas and that for thermogenic gas is referred to as therm-gas. The blue line is the temperature of sea water from Fig. 7(b). The red line is the geothermal gradient in the seabed. (For interpretation of the references to colour in this figure legend, the reader is referred to the web version of this article.)

## 6.2. Comparison to the seismic-reflection profile

The bulk resistivity of the sediments depends on various factors, such as porosity, pore fluid salinity and saturation, mineralogy and the grain fabric of the host sediments (Ellis et al., 2010), which are poorly known for the study area. **The seismic reflection data, co-located with our MCSEM profile, can provide some constraints to aid in the interpretation of the inversion model in Fig. 12.** // 【 (1) 研究主要活动的总结】

**The vertical resistivity model from VTI inversion is overlapped on the seismic reflection section (Fig. 13). For displaying the details, it is exaggerated in a vertical direction. The thin solid line is the resistivity contour of  $3.0 \Omega \text{ m}$ . We can see that the seabed is nearly parallel to the seafloor and that there are three strong seismic reflection events at a depth of approximately 1.67 km in the middle section. These seismicreflection polarities are opposite to those of the seafloor. However, the**

characteristics of the blank seismic reflection are not obvious above the strong reflections. // 【(2) 回顾重要发现】 It is difficult to identify which is the BSR on the seismic-reflection profile. Integrating the thermodynamic calculation (Fig. 12) and the overlapping section (Fig. 13), we infer that the BSR should be the strong reflection event extending transversely from 1.0 to 2.7 km and at a depth of 1.67 km (purple dashed line in Fig. 13), which also consistent with the bottom of layer L2.

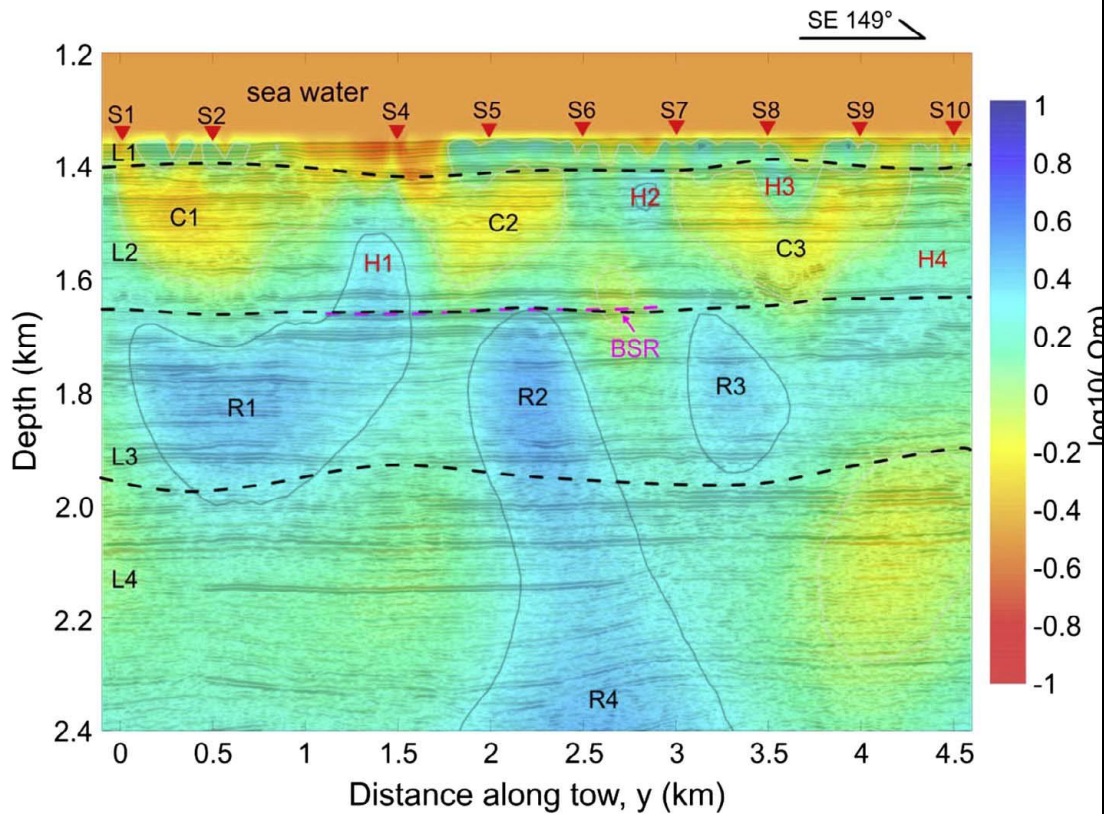


Fig. 13. MCSEM result shown in Fig. 11 overlapped by a seismic profile. However, it is exaggerated in the vertical direction compared to Fig. 11. The black solid thin line is the resistivity contour of  $3.0 \Omega \text{ m}$ , the black dashed lines are the resistivity interfaces and the purple dashed line is the deduced BSR.

Gas hydrate is similar to ice in its high resistance characteristics. Above the inferred BSR, the resistors in the GHSZ (H1–H4 in Fig. 11) correspond to weak and discontinuous seismic reflection events (Fig. 13). We infer that these resistors should be related to gas hydrates.

The resistivity of the seabed is related to ion concentration. When gas hydrates are dissociated, the pore water of the gas hydrate-bearing sediment freshens. This

freshening of pore water can be used to estimate gas hydrate saturations (Wang et al., 2011). In turn, it will be expected that chloride ions would be excluded during hydrate crystallization (Du Frane et al., 2015). Therefore, gas hydrate formation will cause an increase in chloride ion concentration in the surrounding seabed, which can result in a reduction in seabed resistivity. The conductive structures C1, C2 and C3, with a resistivity of approximately  $0.6 \Omega\text{m}$ , are inferred to be real features in layer L2. One of the causes could be that hydrate formation led to increasing salinity in the conductive part. This provides indirect evidence for hydrate formation.

The mass resistors (R1–R4 in Fig. 13) also correspond to weak and discontinuous seismic reflection events. However, because they are below the GHSZ, they may be related to the gas-bearing seabed. //【(3)对于发现的解释】This implies that the underlying strata can provide a gas source for hydrate. Considering the depth of the BSR is consistent with the GHSZ of biogenic methane, we can infer that the natural gas of hydrates can be originally generated from, or partly from, a microbial source below the GHSZ.// 【(5)研究的含义】

## 2.5.2

We have developed a simple method for incorporating seismic constraints into EM inversion through the use of special regularization weights. This seismic regularization method is conceptually similar to MGS regularization in that it produces blocky or sharply focused models. However, unlike the MGS method, it does not suffer from the resistivity-thickness product ambiguity because the structural boundary depths are constrained by the seismic full-waveform inversion model. This approach provides a formal method for the inclusion of seismic structure into EM inversion but avoids the complexities of true joint-inversion methods. // (研究结果)

Test examples show that where resistivity and velocity variations are coincident, the seismically regularized CSEM inversions **can** more accurately recover the resistivity of hydrocarbon layers than standard smooth regularization or MGS regularization. This approach **can** be used to reduce seismic ambiguity, where a target structure identified in the seismic model can be tested for a resistivity anomaly with CSEM inversion. The ability to more accurately resolve the target resistivity also allows for improved estimates of hydrocarbon saturation from CSEM data. // 【研究意义】

The use of seismic velocity gradients to form the regularization weights for the CSEM inversion is just one example of a more general technique. Regularization weights could also be derived from any high-resolution data set that is a priori assumed to be structurally correlated with the CSEM resistivity. Although we have concentrated primarily on seismic full-waveform inversion models due to their high fidelity, nearby well logs and other data sets could also be used. Our test examples included correlated and uncorrelated seismic and electrical structure and showed the method to work best when the structures are correlated with large contrasts in velocity and resistivity.// 【研究结果】 We also find that the method is relatively insensitive to depth errors of 100–200 m in the seismic velocity model, with the resulting seismically regularized CSEM inversion still recovering peak resistivities close to the true value. This approach was shown to perform poorly when the seismic and resistivity structures are strongly uncorrelated, but in such instances, the offset depths between the resistivity and seismic structures will verify that correlated structure required for seismically regularized inversion is not present.

There are limitations to the extent of any improvement in CSEM inversion models from using seismic regularization. For example, because CSEM data are not sensitive to very fine-scale layering, it is unlikely that seismic regularization will improve the resolution of such structures. Additionally, thin multiple stacked reservoir layers or very heterogeneous models with equivalent EM responses will be difficult to resolve due to non-uniqueness, even if the boundaries are well

characterized by seismic velocity gradients. Although we have limited our tests to 1D models, we find no reason the method could not be applied to 2D and 3D modeling when resistivity and velocity are expected to be correlated.// 【不足之处及对于未来工作的建议与展望】

## 2.6 题目与摘要

### 2.6.1

- (1) 1.短语; 2.超过; 3. CSEM-regularized seismic velocity inversion;
- (2) 1.短语; 2.未超过; 3. Seismic facies analysis;
- (3) 1.短语; 2.未超过; 3. Deep-learning inversion;
- (4) 1.问题; 2.未超过; 3. interfacial regime.

### 2.6.2

- (1) (2)

The Qiongdongnan Basin (QB) (研究活动范围) is an important prospecting area for gas hydrates in the South China Sea (SCS). However, it is difficult to infer gas hydrates using a bottom simulating reflector (BSR) under the influence of flat seabed, multiples and bubble effects. In the QB, the upper limit of the gas hydrate stability zone (GHSZ) and the distribution of gas hydrates in the shallow seabed are still not well understood. // (背景信息) A marine controlled-source electromagnetic (MCSEM) survey was completed in order to collect electric resistivity information along a 4.5-km profile. Electromagnetic data were acquired and processed at nine sites. The seafloor receiver orientations were evaluated using the orthogonal procrust rotation analysis (OPRA) method. // (研究中使用方法信息) As a result of

isotropic, vertical transverse-isotropic (VTI), and triaxial anisotropic inversion of electric field Pmax data, a 2-D resistivity image of the seabed was presented.// (研究结果) Preliminary results show that the shallow seabed can be divided into four electric layers. According to thermodynamic conditions in the QB, the estimated thickness of GHSZ is approximately 320 m for biogenic methane and 272 m for thermogenic gas in the study area. The BSR and hydrates were interpreted by integrating the resistivity model along with thermodynamic calculation and seismic reflection data. The MCSEM result indicates there are abundant natural gas originating or partly originating from a microbial source beneath the GHSZ.// (结论陈述)

### 2.6.3

(1) 摘要2的可读性更高，摘要1对于研究背景的描述占据全文较大篇幅，所以相比之下，重点放在介绍本文研究内容与结论的摘要2可读性更高，更能简洁清晰地概括出文章的思路、创新点及结论。

(2)

#### 摘要1

Spatial data mining, i.e., discovery of interesting characteristics and patterns that may implicitly exist in spatial databases, is a challenging task due to the huge amounts of spatial data and to the new conceptual nature of the problems which must account for spatial distance. Clustering and region oriented queries are common problems in this domain. Several approaches have been presented in recent years, all of which require at least one scan of all individual objects (points). Consequently, the computational complexity is at least linearly proportional to the number of objects to answer each query.// (研究背景) In this paper, we propose a hierarchical statistical information grid based approach for spatial data mining to reduce the cost further.// (研究的主要活动) The idea is to capture statistical information associated

with spatial cells in such a manner that whole classes of queries and clustering problems can be answered without recourse to the individual objects. // (研究使用方法信息) In theory, and confirmed by empirical studies, this approach outperforms the best previous method by at least an order of magnitude, especially when the data set is very large.// (研究结果)

## 摘要2

There is often the need to update an installed Intrusion Detection System (IDS) due to new attack methods or upgraded computing environments. Since many current IDSs are constructed by manual encoding of expert security knowledge, changes to IDSs are expensive and slow. // (研究背景) In this paper, we describe a data mining framework for adaptively building Intrusion Detection (ID) methods. // (研究主要活动) The central idea is to utilize auditing programs to extract an expensive set of features that describe each network connection or host session, and apply data mining programs to learn rules that accurately capture the behavior of intrusions and anomaly activities. These rules can then be used for misuse detection and anomaly detection. Detection models for new intrusions or specific components of a network system are incorporated into an existing IDS through a meta-learning (or co-operative learning) process, which produces a meta detection model that combines evidence from multiple models. We discuss the strengths of our data mining programs, namely, classification, meta-learning, association rules, and frequent episodes. // (研究中使用方法) We report our results of applying these programs to the (extensively gathered) network audit data form the DARPA Intrusion Detection Evaluation Program.// (研究结果)